Results in Engineering 29 (2026) 108483

Contents lists available at ScienceDirect

Results in Engineering

journal homepage: www.sciencedirect.com/journal/results-in-engineering

Research paper

Seasonal study of radon concentrations in a uranium mine: A CFD comparison between natural and forced ventilation

Marcos Suárez-Vázquez [a,b,c], Vanesa Somoza [c], Sylvana Varela Ballesta [a,d], Alberto Otero-Cacho [b,c], Alberto P. Muñuzuri [b,c], Daniel Rábago [e], Santiago Celaya [e], Jorge Mira [f,*]

[a] Ventilatio Lab S.L, 15782, Santiago de Compostela, Spain
[b] Galician Center for Mathematical Research and Technology (CITMAga), 15782, Santiago de Compostela, Spain
[c] Group of Nonlinear Physics, Universidade de Santiago de Compostela, 15782, Santiago de Compostela, Spain
[d] Universitat Rovira i Virgili, Departament d'Enginyeria Mecànica, 43007, Tarragona, Spain
[e] Laboratory of Environmental Radioactivity (LaRUC), University of Cantabria, 39011, Santander, Spain
[f] Applied Physics Department and iMATUS, Universidade de Santiago de Compostela, 15782, Santiago de Compostela, Spain

ARTICLE INFO

Keywords:
Radon
CFD
Natural ventilation
Forced ventilation
Simulation

ABSTRACT

Radon is a naturally occurring radioactive gas that accumulates inside poorly-ventilated environments, posing significant health risks due to its association with lung cancer. This study analyzes indoor radon dynamics in a building located within a former uranium mine in Saelices el Chico (Spain), evaluating the effectiveness of natural and mechanical ventilation for radon mitigation. Experimental measurements were conducted to monitor radon levels over time, supported by a CFD model that simulated both indoor and outdoor environments while accounting for terrain-induced wind effects. This modeling approach improved boundary condition accuracy, revealing up to 20 % discrepancies between raw meteorological data and simulated environments. A seasonal analysis was performed under representative weather conditions and compared with a forced ventilation scenario using an industrial fan to continuously supply fresh air. The mechanical ventilation model showed strong agreement with experimental results. Findings indicate that mechanical ventilation substantially enhances air renewal—reaching up to 2.21 air changes per hour (ACH)—whereas natural ventilation only provides 0.13–0.25 ACH, corresponding to renewal times between 4 and 8 hours. As a result, simulated radon concentrations inside the studied room dropped from over 10,000 Bq/m^3 under natural conditions to about 2,000 Bq/m^3 within just one hour after implementing the mechanical setup. These findings demonstrate the critical role of mechanical ventilation in reducing radon accumulation and improving indoor air quality, particularly in buildings with limited openings, suboptimal airflow paths, or low wind conditions where natural ventilation becomes ineffective.

1. Introduction

Radon (^{222}Rn) is a naturally occurring radioactive element produced by the decay of radium-226 (^{226}Ra) formed along the uranium-238 (^{238}U) decay chain, which is present in varying concentrations in soil, rock, and groundwater [1]. Radon has several isotopes, including ^{220}Rn (thoron) and ^{219}Rn (actinon), but ^{222}Rn is the most relevant for indoor air quality due to its relatively long half-life of 3.8 days [2]. This half-life allows it to accumulate in enclosed spaces such as buildings, whereas ^{219}Rn and ^{220}Rn (with half-lifes of only 4.0 and 55.6 seconds, respectively [3]) decay too quickly to pose a similar threat. However, in some cases, thoron can contribute to indoor radon concentrations, particularly in basements located in areas with high geogenic radon potential or in buildings constructed with materials enriched in thorium [4]. When inhaled, radioactive progeny of radon present in the air, such as ^{218}Po and ^{214}Po, emit alpha radiation that can damage lung tissue and increase the risk of lung cancer. This risk is further enhanced by the exposure to air pollution and smoking [5,6].

According to the European Environment Agency (EEA), radon is responsible for approximately 1 in 10 lung cancer cases in Europe [7], making it a significant public health concern. Only in 2019, around 19,000 lung cancer deaths in Europe may have been due to naturally occurring indoor residential radon [8]. Exposure occurs primarily in homes and workplaces, where radon seeps through foundation cracks, construction joints, and gaps around pipes [9]. Degassing from water with high concentrations of radon is also an important source of radon

* Corresponding author.
E-mail address: jorge.mira@usc.es (J. Mira).

https://doi.org/10.1016/j.rineng.2025.108483
Received 25 August 2025; Received in revised form 18 November 2025; Accepted 28 November 2025
Available online 1 December 2025

in air, and is regulated in Spain by Royal Decree 3/2023 [10], which establishes quality criteria for drinking water. Building materials are also a relevant source of radon and thoron in some cases [11,12]. While their contribution to indoor concentrations is generally low [13], it can become significant or even predominant in specific scenarios—such as in upper-floor dwellings, newly built energy-efficient homes, or historic buildings featuring ultra-thick walls. Given its health risks, effective mitigation strategies are crucial, particularly in high-radon areas.

International regulations on radon exposure have evolved to establish reference levels that protect public health. The European Union's Directive 2013/59/Euratom [14] sets a reference level of 300 Bq/m^3 for indoor radon concentrations, applicable to homes, public buildings, and workplaces. However, some European countries, such as Germany [15] and the United Kingdom [16], recommend not exceeding 100 Bq/m^3 and consider levels above 200 Bq/m^3 as a risk. In Spain, Royal Decree 1029/2022 [17] establishes a 300 Bq/m^3 reference level for enclosed spaces, aligning with EU directives. Moreover, the Nuclear Safety Council (Consejo de Seguridad Nuclear, CSN) in Spain has categorized the country's regions based on radon levels, identifying areas where a significant percentage of the population is subjected to radon concentrations greater than 300 Bq/m^3 [18]. Furthermore, the World Health Organization (WHO) suggests that radon concentrations should not exceed 100 Bq/m^3 [19] to minimize significant health risks.

Effective mitigation strategies are crucial for reducing radon exposure [20,21], particularly in areas with high radon potential. The simplest strategy consists in increasing natural ventilation [22], which helps reducing indoor radon levels by promoting the exchange of indoor and outdoor air, preventing the gas from accumulating in enclosed spaces. This strategy, however, is not always effective due to geometrical considerations or predominant wind conditions, and its applicability in residential buildings and workspaces may be further constrained during colder periods, when the need to preserve indoor thermal comfort and energy efficiency limits the extent of natural ventilation. In parallel, mechanical ventilation can be applied to increase air exchange in a more controlled way, offering a practical alternative when natural ventilation alone is insufficient [23]. Another common technique involves sealing cracks in floors and walls [24], thus preventing radon from seeping into buildings. Additionally, radon sumps or sub-slab depressurization systems [25] can be installed to lower the pressure beneath the foundation, effectively redirecting radon gas before it enters indoor spaces. These last two alternatives are often associated with projects that are difficult to execute or restricted by legislation, making both natural and mechanical ventilation highly relevant options in many cases [26].

To optimize these mitigation strategies, Computational Fluid Dynamics (CFD) simulations provide valuable insights by modeling radon transport and accumulation under different ventilation scenarios and environmental conditions [27,28]. These simulations enable a detailed assessment of airflow patterns and radon dispersion, helping to refine mitigation techniques to improve indoor air quality. Moreover, CFD-based studies contribute to the development of more efficient ventilation designs, ensuring that mitigation measures are both effective and energy-efficient.

Previous studies have analyzed the effects of temperature differences between indoor and outdoor environments [29,30], as well as the influence of external meteorological conditions and wind direction across various window geometries [31]. However, many of these works face limitations in the way boundary conditions are defined, often simplifying or neglecting the outdoor environment and local orography. For example, [30] determinates inlet velocities based on experimental measurements of radon concentrations rather than deriving them from external meteorological data or predictive models, while other studies [32] do not explicitly specify how inlet velocities are implemented. These simplifications become even more critical in urban settings, where surrounding buildings strongly influence airflow patterns and, consequently, the accuracy of predictive indoor ventilation simulations. Moreover, many of these studies lack validation through real-life measurements, limiting the reliability of their CFD simulation results.

The existing bibliography on CFD simulations of radon transport remains limited, with most studies focusing on simplified or idealized boundary conditions and rarely accounting for the complexity of real environments. To address these issues, we present a modeling approach for a real building and its surrounding environment, supported by precise radon concentration measurements performed in an old uranium mine, a unique experimental building in Salamanca, Spain. To achieve a comprehensive analysis that accounts for general seasonal conditions, averaged wind parameters were selected and incorporated into an automated tool designed to simulate wind currents using low-resolution wind data. This approach considers the influence of buildings, vegetation, bodies of water, and terrain elevation [33], raising a more realistic value of the real wind speed and direction. The resulting wind measurements from these simulations are then employed as boundary conditions for the radon ventilation simulations, in which the time evolution of radon concentration levels is analyzed and compared. Finally, a forced ventilation system is implemented in the CFD simulations and evaluated in comparison with the experimental measurements.

This paper is structured as follows. Section 2 outlines the methodology, detailing the geometry preparation and the simulation setup. A brief discussion of the selected wind conditions is presented, along with an evaluation of the CFD-based reconstruction of the surrounding terrain to the studied building. Then, results for every seasonal simulation are presented in Section 3, and a comparison between them is performed. Lastly, a forced ventilation system is introduced within the simulation, comparing the radon concentration levels to real-world measurements.

2. Methodology

2.1. Numerical simulations using CFD techniques

Independent numerical simulations were carried out to analyze air circulation inside and outside the experimental building. The commercial software Simcenter STAR-CCM+ [34] was used to design the building geometry, build the polyhedral meshes, solve the governing conservation equations (Navier-Stokes) using Finite Volume Methods (FVM) [35] and post-process the results. The equations for the conservation of mass and momentum read as,

$$\frac{\partial}{\partial t}\int_V \rho dV + \oint_A \rho \cdot \mathbf{v} \cdot d\mathbf{a} = \int_V S_u dV, \tag{1}$$

$$\frac{\partial}{\partial t}\int_V \rho \mathbf{v} dV + \oint_A \rho \mathbf{v} \otimes \mathbf{v} \cdot d\mathbf{a} = -\oint_A p\mathbf{I} \cdot d\mathbf{a} + \oint_A \mathbf{T} \cdot d\mathbf{a} + \int_V \mathbf{f}_b dV + \int_V \mathbf{s}_u dV, \tag{2}$$

where t is time, V is volume, $\mathbf{a}$ is the area vector, ρ is the density, $\mathbf{v}$ is the velocity, p is pressure, $\mathbf{T}$ is the viscous stress tensor, $\mathbf{I}$ is the isotropic pressure force contribution from the total stress tensor $\boldsymbol{\sigma} = -p\mathbf{I} + \mathbf{T}$, $\mathbf{f}_b$ is the resultant of body forces, S_u, s_u are user-specified source terms, and $\otimes$ denotes the outer product.

An incompressible solver with constant density was selected, along with a realizable k-ε turbulent Reynolds-Averaged Navier-Stokes (RANS) model, which has been widely adopted for numerical simulations of air circulation and pollutant dispersion in enclosed environments [36]. This model offers a good compromise between accuracy and computational cost, and has been successfully applied in several recent CFD studies of indoor radon transport and ventilation performance [37,38], demonstrating its capability to capture realistic mixing and ventilation patterns under typical indoor Reynolds numbers. In addition, an enhanced wall treatment with a two layer approach [39] was used to gain flexibility of an all $-y^+$ wall treatment.

The transport equations for the kinetic energy k and the turbulent dissipation rate ε of the turbulence model are given as in Eqs. (3) and (4),

Table 1
Properties of the two species for the multi-component gas [40].

	Air	Radon
Density (kg/m^3)	1.26	9.73
C_p (J/kg·K)	1003.62	93.55
Dynamic Viscosity (kg/m·s)	$1.86 \cdot 10^{-5}$	$2.45 \cdot 10^{-5}$
Molar weigth (kg/kmol)	28.97	222.02

$$\frac{\partial}{\partial t}(\rho k) + \nabla \cdot (\rho k \overline{\mathbf{v}}) = \nabla \cdot \left[\left(\mu + \frac{\mu_t}{\sigma_k}\right)\nabla k\right] + P_k - \rho(\varepsilon - \varepsilon_0) + S_k, \tag{3}$$

$$\frac{\partial}{\partial t}(\rho \varepsilon) + \nabla \cdot (\rho \varepsilon \overline{\mathbf{v}}) = \nabla \cdot \left[\left(\mu + \frac{\mu_t}{\sigma_\varepsilon}\right)\nabla \varepsilon\right] + \frac{1}{T_\varepsilon} C_{\varepsilon 1} P_\varepsilon - C_{\varepsilon 2} f_2 \rho \left(\frac{\varepsilon}{T_\varepsilon} - \frac{\varepsilon_0}{T_0}\right) + S_\varepsilon, \tag{4}$$

where $\overline{\mathbf{v}}$ is the mean velocity; μ is the dynamic viscosity; $\sigma_k = 1.0$, $\sigma_\varepsilon = 1.2$, $C_{\varepsilon 1} = 1.44$, and $C_{\varepsilon 2} = 1.9$ are the model coefficients; f_2 is a damping function; and S_k, S_ε are the user-specified source terms. The subscripts in ε_0, T_0 indicate baseline values for dissipation and time scales. P_k and P_ε are the production terms defined by Eqs. (5) and (6),

$$P_k = f_c G_k + G_b - \gamma_M, \tag{5}$$

$$P_\varepsilon = f_c S_k + C_{\varepsilon 3} G_b, \tag{6}$$

where $C_{\varepsilon 3} = \tanh(|v_b|/|u_b|)$ is a model coefficient in which u_b and v_b are the velocity components parallel and perpendicular to the gravitational vector $\mathbf{g}$, f_c is the curvature correction factor, G_b and G_k are buoyancy and turbulent production, γ_M is the compressibility modification [41], $f_2 = k/\left(k + \sqrt{\nu\varepsilon}\right)$ is a damping function and $S_{k,\varepsilon}$ are the user-defined source terms.

SIMPLE algorithm was used for pressure-velocity coupling and a second-order upwind discretization scheme was used for the conservation of mass and momentum equations. The influence of temperature and relative humidity in the radon exhalation rate was not considered in this study, as we will explain later.

For representing radon concentrations, a multi-component gas model was used, with two different species: air and radon gas. The selected physical properties for each species used in the transport equations are presented in Table 1. The transport equation for the mass fraction Y_i of a species is given by Eq. (7),

$$\frac{\partial}{\partial t}\int_V \rho Y_i dV + \oint_A \left[\rho Y_i(\mathbf{v} + \mathbf{M}_i)\right] \cdot d\mathbf{a} = \oint_A \left[\mathbf{J}_i + \frac{\mu_t}{\sigma_t}\nabla Y_i\right] \cdot d\mathbf{a} + \int_V \left(S_{Y_i} + C_i\right) dV \tag{7}$$

where $\mathbf{M}_i$ is the migration term included when modeling the movement of charged species, σ_t is the Schmidt number, $\mathbf{J}_i$ is the diffusive flux and C_i is the added transport term when modeling concentrated charge migration.

2.2. Radon measurements and place of study

The experimental data used to calculate the radon generation rate was measured at the Laboratory of Natural Radiation (LNR)[1], a unique experimental building located at the former uranium mine managed by *ENUSA Industrias Avanzadas* in Saelices el Chico, Salamanca, Spain (see Fig. 1). Experimental data was measured during the "International Intercomparison Exercise on Natural Radon Radiation Measurements Under Field Conditions 2024", a reference activity for radon measurements celebrated in May 20–23, 2024.

The suitability of this environment for such activities is attributed to the high content of radioactive elements present in the soil, together with the site-specific environmental conditions. Measurements were conducted in **Room 1**, marked as a red prism in Fig. 1(a), which has a total volume of 56.91 m^3. The only connection between Room 1 and the external environment is a pressurization system, which was completely deactivated during the measurement period. Room 1 is connected to the rest of the LNR building via a completely sealed metal door facing east. Said building has a metallic door facing south that provides access from the outside. Given that the pressurization system was deactivated, ventilation of Room 1 is only possible when both doors are open. A general overview of the real and reconstructed domains can be seen in Fig. 1, with the inclusion of the mechanical ventilation system used later.

Measurements were taken every 10 minutes using an AlphaGUARD radon monitor, whose technical characteristics are shown in Table 2. The monitor was calibrated in the calibration chamber of the Laboratory of Environmental Radioactivity of the University of Cantabria (LaRUC) [42–44], which is accredited according to UNE-EN ISO/IEC 17025:2017 [45].

Prior to the initiation of radon exposure measurements, the intrinsic background signal of the monitor was determined. This background represents the average radon concentration recorded by the device in the absence of an external radon source and arises due to electronic noise or residual contamination from long-lived radionuclides [46,47]. To ensure accurate environmental radon measurements, this background value must be subtracted from each recorded data point, as it does not reflect the actual radon concentration in the monitored environment. The determined background level of the monitor was found to be 103 Bq/m^3.

The measurements were conducted in Room 1 of the LNR for a continuous span of 4 days, between May 20–23, 2024. Fig. 2 shows the evolution of radon concentration, measured in Bq/m^3. The sensor was placed in the middle of the room at 1 m high, over a table of size 2.5 × 1.0 m. The room remained completely sealed during the entire process, with no direct clean air ingress during the experiment.

2.3. Analytical model: radon balance equation

The time evolution of the average radon concentration within an enclosed space is governed by a balance equation [48],

$$\frac{dC(t)}{dt} = \frac{G}{V} - \left(\frac{\phi}{V} + \lambda_{Rn}\right) C(t), \tag{8}$$

where C (Bq/m^3) is the average radon concentration in the room, V (m^3) is the room volume, ϕ (m^3/s) is the volumetric air exchange rate (both from ventilation and air leakages), and λ_{Rn} (s^{-1}) is the radon decay constant. The source term G (Bq/s) represents the total radon entry rate into the room, which is often derived from the radon exhalation rate per unit surface area E (Bq/m^{2}s) and the surface area A (m^2) of the enclosing walls and floor, so that $G = E \cdot A$.

In practice, this radon exhalation rate $G(t)$ is not strictly constant but often exhibits a time dependence driven by external meteorological conditions. $G(t)$ can be regarded as consisting of two main components: one that varies dynamically with environmental and indoor parameters such as pressure, temperature, and humidity [49,50]; and another that reflects a baseline contribution ensuring the system tends toward its characteristic equilibrium state. This perspective can be loosely interpreted in analogy with a mean-field approach, where the baseline term acts as a restoring force. For instance, in a completely ventilated room with negligible radon concentration, this contribution would initially be dominant, driving the concentration upward to an expected equilibrium value. As this steady state is approached, the baseline contribution starts becoming smaller, and the fluctuations caused by the meteorologically driven component—which can be either positive or negative—play a more significant role, thereby explaining the observed variability in indoor radon concentration. Formally, this can be expressed as

$$G(t) = G_b(C(t)) + G_{\text{met}}(t), \tag{9}$$

[1] The exact coordinates of the building are: 40°38′13.0"N, 6°36′55.0"W.

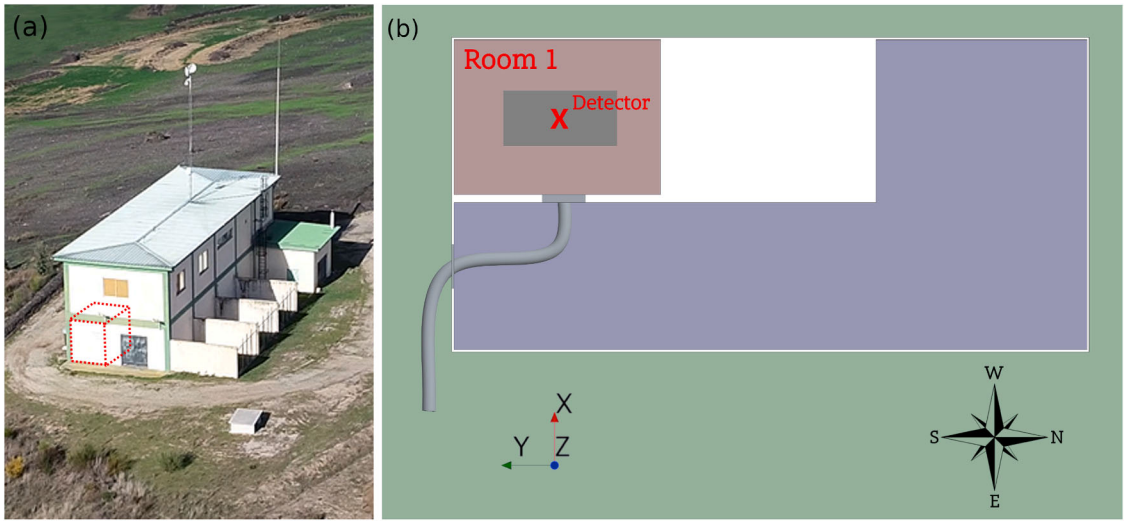

Fig. 1. (a) Aerial view of the LNR, showing the studied room marked in red. (b) Reconstructed geometry of the LNR building inside the simulation software. The detector position is marked with a red cross, and the system used in the mechanical ventilation simulation is shown with a gray tube. (For interpretation of the references to colour in this figure legend, the reader is referred to the web version of this article.)

Table 2
Technical characteristics of the radon monitor used in the study.

Device name	Manufacturer	Detection principle	Range (Bq/m^3)	Sensitivity (cpm at 1 kBq/m^3)	Radon uncertainty (statistical)
AlphaGUARD	Bertin Instruments (Frankfurt, Germany)	Pulsed Ionization Chamber	$2 - 2 \cdot 10^6$	50	$< \pm 10\,\%$ at 200 Bq/m^3 after 1 h

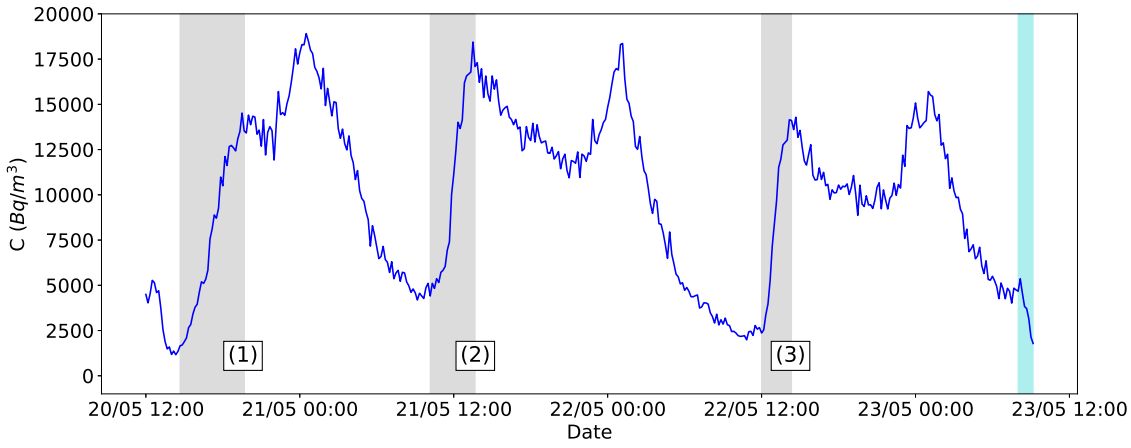

Fig. 2. Radon concentration in Room 1 on May 20–23, 2024. The gray areas indicate the intervals used for extracting a generation rate using a linear fit. A measurement with forced ventilation was performed at the end of the period and is shown in the blue area, during which both doors of the building were opened. In all other cases, Room 1 was kept fully sealed to ensure isolation from external influences. (For interpretation of the references to colour in this figure legend, the reader is referred to the web version of this article.)

where $G_b(C(t))$ denotes the baseline restoring term which dominates at lower radon concentrations and $G_{\text{met}}(t)$ represents the meteorologically driven fluctuations, explaining why radon concentrations can still decrease in enclosed spaces without significant ventilation.

In our case, the available experimental data does not correspond to conditions starting from a low-concentration, ventilated environment, but rather to situations in which the fluctuating component of the generation rate is already dominant. As a result, it is not possible to fit the measurements to the baseline equilibrium and directly extract a representative generation rate for modeling the growth of radon concentration from a ventilated condition. For that reason, we adopt a different strategy: we neglect the baseline contribution and focus on the regions of the experimental data that correspond to worst-case scenarios. By fitting the solution of Eq. (8) to these selected regions, we can obtain reference values for the maximum values of the fluctuating component, $G(t) \simeq G_{\text{met}}(t)$, which can then be employed to simulate ventilation strategies under worst-case conditions, a common approach in this type of risk prevention studies.

Following this, we can define the Air Changes per Hour (ACH), which represents the number of times the air inside the room is exchanged per unit time,

$$\lambda_{ACH} \equiv \frac{v_\perp A}{V} = \frac{\phi}{V}. \tag{10}$$

From this, we can define the equivalent decay constant, that accounts for both the air renewal rate and radioactive decays,

$$\lambda = \lambda_{Rn} + \lambda_{ACH}. \tag{11}$$

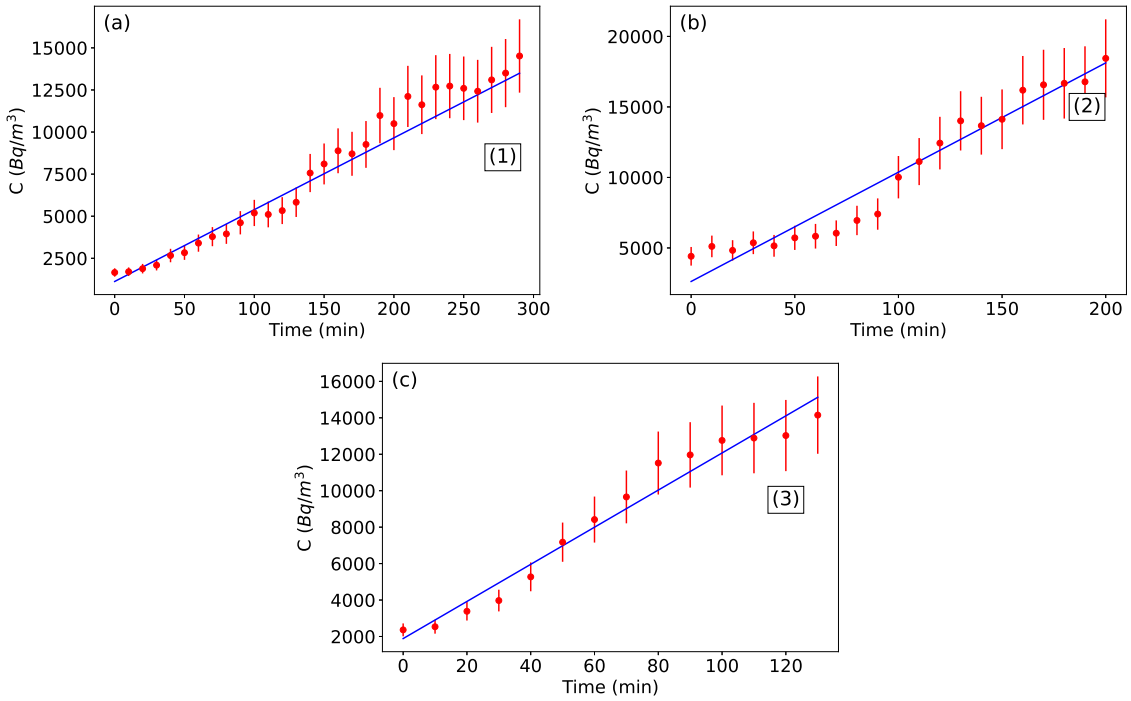

Fig. 3. Experimental measurements of radon concentration (red points) compared with radon concentration growth predicted by the model in Eq. (15). Each fit corresponds to the corresponding gray area in Fig. 2. (For interpretation of the references to colour in this figure legend, the reader is referred to the web version of this article.)

Therefore, Eq. (8) can be rearranged into,

$$\frac{dC(t)}{dt} = \frac{G}{V} - \lambda C(t), \tag{12}$$

with the following analytical solution,

$$C(t) = C_\infty + (C_0 - C_\infty)e^{-\lambda t}, \tag{13}$$

where $C_0 = C(t = 0)$ is the initial condition of radon concentration and $C_\infty = G/\lambda V$ represents the equilibrium concentration where the rate of input G/V exactly balances the rate of removal λC. In our measurements, the room was considered nearly airtight, such that $\lambda_{ACH} \simeq 0$. For relatively short observation periods, we can also neglect the radioactive decay constant λ_{Rn} compared to the rate of change of $C(t)$. Under these assumptions, Eq. (12) reduces to

$$\frac{dC(t)}{dt} = \frac{G}{V}, \tag{14}$$

whose analytical solution can be written as

$$C(t) = C_0 + \frac{G}{V}t, \tag{15}$$

which is a straight line with initial condition C_0 and slope equal to G/V. This means that, in complete absence of air renewal, the radon concentration grows in a straight line, transitioning to an exponential trend when air leaks are considered. Knowing the volume of the place, we can adjust the experimental values to get a representative value for worst-case scenarios of the meteorologically-driven radon generation rate, which we will then use in our simulations. These scenarios are marked in gray in Fig. 2. As we are considering long time series spanning several hours (150–300 minutes), some deviations from the straight-line behavior of the radon concentration are to be expected, since these intervals are long enough for external meteorological conditions to vary and influence the radon generation rate. The corresponding linear fits during the three measurement intervals are shown in Fig. 3. Each 10-minute measurement is assigned an uncertainty of ±15 % of its value, consistent with the AlphaGuard's specified statistical performance for short averaging intervals.

Table 3
Extracted values for G from the linear fits.

Interval	1	2	3	Average
G (Bq/s)	40.5 ± 1.5	73.5 ± 4.0	96.6 ± 5.3	70.2 ± 2.3

The radon concentration fits exhibit some oscillations, with three distinct cases that have been fitted using a linear approximation of the balance equation, as in Eq. (15). Although the concentration does not increase monotonically over the four days of measurement—fluctuating substantially instead—the calculated exhalation rates G are considered to be important for risk prevention. As explained, this approach assumes a worst-case scenario by modeling an effective source term that drives the concentration upward, despite the natural variability in exhalation rates over time due to humidity, pressure and temperature changes [51]. The extracted values for the generation rate are shown in Table 3. The average G value was chosen as a reference value for our simulations, even taking into account the notably different values extracted from the linear fits.

The usage of linear fits is justified by the conditions under which Eq. (15) is valid. Room 1 is completely sealed from the rest of the building, making air exchange completely negligible. The variability in radon concentration observed in the experimental data shown in Fig. 3 can be explained by the long time intervals considered, during which the meteorological component of the exhalation rate can vary substantially. Exponential fits with $\lambda \neq 0$ were also tested, but they didn't provided better agreement with the experimental data.

2.4. Meteorological conditions

To conduct our simulations, we selected the most representative meteorological conditions for each season. Historical wind data spanning over a decade was obtained from OpenMeteo [52], using measurements recorded at the nearest meteorological station, located approximately 4 km away from the study area. The data was categorized by season to

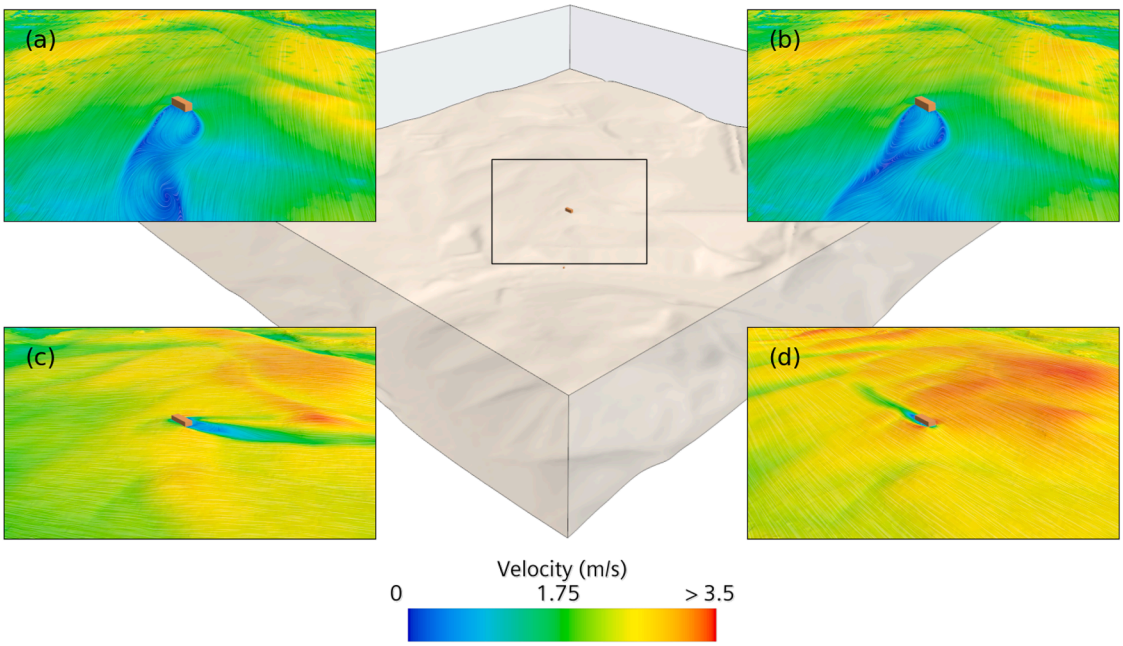

Fig. 4. Reconstructed domain around the LNR laboratory. The building is located in the center of the domain, and the wind direction and speed is measured 50 m from it in a direction parallel to the wind movement. The velocity field at 2 m height is shown for each season: (a) Winter, (b) Spring, (c) Summer and (d) Autumn.

Table 4
Comparison between the meteorological station data and the CFD reconstruction results of wind speeds and directions. Both values are referenced at 10 m height.

	Winter		Spring		Summer		Autumn	
	Station	CFD	Station	CFD	Station	CFD	Station	CFD
Wind speed (m/s)	2.7	2.4	2.8	2.5	2.5	2.5	2.5	3.0
Wind direction (°)	45.0 (NE)	45.6	45.0 (NE)	45.7	315.0 (NW)	315.2	180.0 (S)	177.1

facilitate the analysis. The wind direction histogram demonstrated distinct distributions, with prevalent wind directions varying across seasons, while the wind velocity magnitude frequencies exhibited consistent seasonal trends. Both histograms are included in the Supplementary Material.

These simulations were designed to isolate the impact of seasonal wind patterns. Therefore, inputs were based on the dominant wind speed and direction for each season. While seasons also involve changes in other variables, these are not relevant to the scope of this study as they do not influence the results of the simulations.

To determine the most representative wind speed and direction at a height of 10 m, we extracted the median wind velocity and the most frequently observed wind direction for each season, as summarized in Table 4. The selected wind values correspond to measurements taken at a meteorological station positioned 10 m above ground level in a small town near the study site. However, these values do not necessarily represent the wind conditions affecting the LNR laboratory. To address this discrepancy, we employed an automated CFD tool, validated in [33], to reconstruct high-precision wind fields in the study area while incorporating the influence of buildings and vegetation from low-resolution wind data. The registered value at 10 m in the vicinity the laboratory is displayed in Table 4, and compared to the value extracted from the meteorological station.

In our analysis, we assumed that the wind speed recorded at the meteorological station was comparable to that of the study area, despite the 4 km separation. Additionally, we accounted for terrain elevation to accurately estimate the wind speeds impacting the vicinity of the LNR laboratory.

This methodology ensures the preservation of the neutral atmospheric boundary layer logarithmic profile by applying appropriately corrected boundary conditions in the CFD simulations. Consequently, the resulting wind speed values near the building at a specified height can be used as a reference for the boundary conditions for radon dispersion simulations. Fig. 4 presents the reconstructed domain surrounding the LNR laboratory along with the different simulations. A more complete representation of the wind fields in the whole domain is provided in Figures S3, S4, S5, and S6 of the Supplementary Material.

As it can be seen, in only one of the four cases (Summer) the wind speed registered in the simulation near the laboratory is comparable to the one extracted from the meteorological station situated far away. The other three cases show a difference of more than 15 % between both speed values, demonstrating the usefulness of this methodology to estimate the wind currents near the building. The wind direction value is almost identical for the four cases, which was to be expected given the location of the building, with no disturbances modifying the air patterns other than the terrain elevation. This tool could become even more powerful in more complex environments, where the presence of larger vegetation zones or more buildings could really affect the behavior of wind patters, raising even larger differences in relation to the meteorological station values, for both wind speed and direction. The simulated values at 10 m height presented in Table 4 will be used as a reference for the inlet boundary conditions in all our radon simulations.

2.5. Numerical domain and boundary conditions

As marked before, the study is not limited to the interior of the building, as we only have one door connecting it to the outside. For that reason, the setting of appropriate boundary conditions becomes harder, as fresh air should be entering and exiting at the same boundary, complicating the setup of the simulation. For that reason, an exterior domain

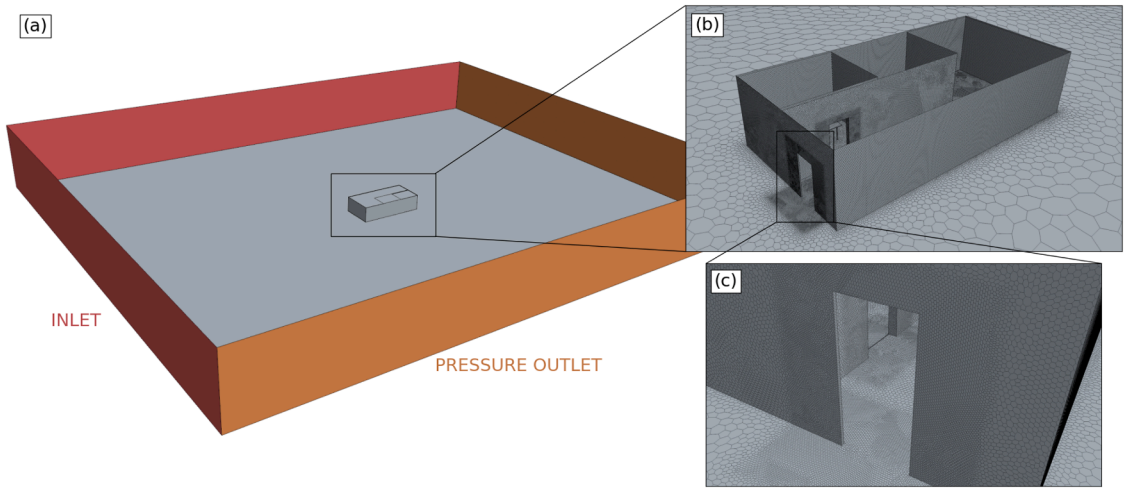

Fig. 5. (a) Exterior domain of the building with example inlet positions and (b) selected mesh for the simulations. (c) The mesh was refined near the building and, specifically, close to the doors.

surrounding the building shown in Fig. 5(a) was considered. The sizes of the exterior domain follow the recommended dimensions in [53], with a blockage ratio (BR) of less than 3 %, that effectively limits the border effects in the simulation and the artificial acceleration of wind. The outside region is considered to be flat, as the terrain elevation has already been considered in the reconstructions from the previous section.

A mesh independency test was performed to assess the suitability of the numerical domain, and all the extracted numerical results can be further examined in the Supplementary Material. We considered three starting meshes (Fine, Intermediate and Coarse) with different sizes and variable refinements inside the building and near the doors. We found out that the results were not consistent between these three starting meshes, as the final average concentration inside the building and the Room 1 had up to 10 % of difference between meshes. A fourth one with more refinement near the doors was considered, raising a similar result than the Fine mesh, but with an increase of over 50 % of cells and computational time. For that reason, we finally decided to use the Fine mesh, as it represented a good tradeoff between the number of cells (computational time) and the precision of the results. An overview of the selected mesh can be seen in Fig. 5(b,c), and the most relevant parameters are shown in Table 5. The selected mesh is configured using a Base Size of 1.25 m, and two volumetric controls for the proximity of the building and the interior of Room 1.

As explained before, we performed the reconstruction of the environment with the aim of fine-tuning the boundary conditions of our ventilation simulations, whose results can be seen in Table 4. We will use the value at 10 m height extracted from the reconstruction as a reference for the radon simulation, also modeling the atmospheric boundary layer logarithmic profile [54] at every point. This equation states that the wind velocity at any height can be expressed in terms of the height with respect to the ground as in Eq. (16),

$$v(z) = \frac{u_*}{\kappa} \log\left(\frac{z + z_0}{z_0}\right), \tag{16}$$

where $\kappa = 0.41$ is the von Karman constant [55], z is the height, $z_0 = 0.1$ is the aerodynamic roughness length that depends on the type of terrain [56], and u_* is the friction velocity, whose value can be extracted by knowing the wind velocity at a given height. This equation is used for the boundary conditions of the four simulations. For the cases with diagonal wind (NE, NW), two walls were set as inlets, while for the case with south wind (S), only one was considered. The other lateral walls were set as pressure outlets, while the rest of the domain has a no-slip wall boundary condition. Inside the building model, radon exhalation was applied only on the floor of Room 1 for simplification, as this required less mesh refinement. The emission rate assigned to the floor corresponds to the average radon generation rate derived from the linear fits in Fig. 3, equal to 71.9 Bq/s. This is equivalent to a flux of $7.64 \cdot 10^{-19}$ kg/m^{2}s, as detailed in the Supplementary Material. Distributing the same total exhalation over both the floor and the lateral walls would yield similar results, as the total radon exhalation rate would remain unchanged.

2.6. Forced ventilation

To improve the inflow of clean, radon-free air into Room 1, a forced ventilation system was installed on the last day of measurements. Following its installation, radon concentration measurements were taken to establish a reference curve for the decrease in radon levels. The area highlighted in blue in Fig. 2 represents the time interval, conducted between 8:00 and 9:00 AM on May 23rd.

During this interval, we calculated the average wind velocity and direction recorded by the nearest meteorological station. As in previous analyses, we simulated the reconstructed domain surrounding the LNR building and extracted localized wind velocity and direction near the structure to serve as boundary conditions for the ventilation simulation. The wind speed used in the simulation was 2.91 m/s, with a direction of 33.5° (close to northeast, NE). In contrast, the meteorological station reported a wind speed of 2.51 m/s and an almost identical direction of 34.0°. This discrepancy in wind speed highlights once again the intrinsic value of the reconstructed domain around the LNR building, as it allows for more accurate boundary conditions in our radon dispersion simulations.

The ventilation system includes a VEVOR fan (model BT-SHT12A-U(S)5) with a diameter of 12 in. (30.48 cm). To accurately represent the fan's effect in the simulations, a 30.48 cm diameter cylindrical inlet was installed inside the LNR, adjacent to the door of Room 1, as shown in Fig. 1. A mass flow inlet of 0.04 kg/s was placed near the door, with a cylindric tube with an outlet at the other end of the tube.

3. Results

We conducted four distinct simulations, each corresponding to a different season, based on the CFD boundary conditions extracted from the reconstruction presented in Fig. 4. In these simulations, we measured the average radon concentration within the entire LNR building as well as specifically inside Room 1. Since real-life measurements were performed exclusively within Room 1, we obtained a direct estimate of the radon generation rate inside this room but lacked equivalent data

Table 5
Summary of the mesh independency test results. The percentage values represent the difference with respect to the selected mesh for the simulations (Fine).

Mesh	Base Size (m)	Number of cells	Computation time	Final radon concentration LNR (Bq/m^3)	Final radon concentration Room 1 (Bq/m^3)
Fine	**1.25**	**2 242 149**	**1.1 days**	**2163**	**7099**
Intermediate	2.50	567 529	5 hours	2043 (-5.5 %)	6381 (-10.1 %)
Coarse	4.00	217 019	2 hours	2133 (-1.4 %)	6014 (-15.3 %)
Optimized	1.25	3 769 537	2 days	2175 (0.5 %)	7386 (4.0 %)

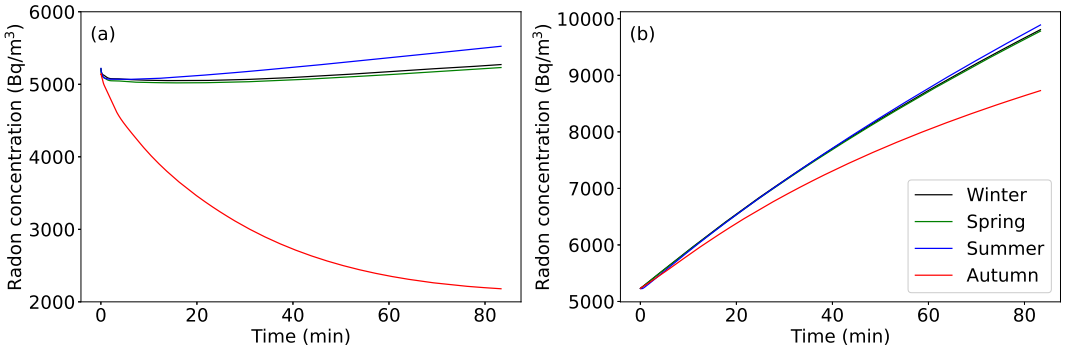

Fig. 6. Time evolution of radon concentration (a) in the entire LNR building and (b) inside the Room 1 for the four seasonal simulations.

for the rest of the building. Consequently, we opted to introduce a radon generation rate solely for the walls of Room 1.

As previously discussed, we can define the radon generation rate G as a value with two different contributions: one that works for lower radon concentrations and the other that oscillates depending on the meteorological conditions. At higher concentrations, the baseline generation rate can be neglected and we have to consider the significant influence of external environmental factors, such as temperature, humidity, and pressure variations. The choice of a relatively high generation rate, neglecting the baseline contribution and adjusting the meteorological generation rate to the intervals in which the rate of change in the concentration is higher, ensures that our analysis accounts for a worst-case scenario. Given the limited influx of fresh air from the exterior, the ventilation intervals needed to achieve lower radon levels are substantially prolonged, making the generation rate a critical factor in the overall radon concentration dynamics. After performing the simulations, we can extract an equivalent ventilation rate ($\lambda \simeq \lambda_{ACH}$) fitting Eq. (13) to the simulated data to quantify the ventilation effectiveness.

The evolution of the radon concentration for the seasonal simulations is presented in Fig. 6, while the λ_{ACH} values for both Room 1 and the whole LNR building are presented in Table 6. Furthermore, an animated video for each simulation is also included in the Supplemetary Material.

An initial uniform radon concentration of 5200 Bq/m^3 was chosen in all the simulations, as it is the initial condition for the forced ventilation measurements marked in blue in Fig. 2. This will serve us as a good reference for the comparison between the natural and forced ventilation mechanisms, as we will see later.

Among the four simulations, only one scenario resulted in a significant reduction in the average radon concentration within the LNR building. However, none of the cases effectively reduced radon levels in Room 1, where a high radon generation rate was imposed.

The results for winter and spring are nearly identical, which was something to be expected given the similar boundary conditions in both cases: the wind direction at the inlet remained equal (NE), and the wind speed difference between both simulations was less than 4 %. This NE wind direction primarily impacts the side of the building opposite the south-oriented door, allowing only low-speed recirculation zones behind the structure to enter the building and contribute to air exchange.

The summer simulation presents a case of symmetry along the E-W axis due to the pure NW wind direction. Initially, one might expect

Table 6
Air Changes per Hour (ACH) for each season inside Room 1 and the whole LNR building.

Season	Winter		Spring		Summer		Autumn	
Region	Room 1	LNR	Room 1	LNR	Room 1	LNR	Room 1	LNR
λ_{ACH} (h^{-1})	0.14	0.17	0.14	0.18	0.13	0.13	0.25	1.11

results to be similar to those of winter and spring; however, as observed in Fig. 6, ventilation worsens slightly. This difference is attributed to the placement of the LNR building's door. As shown in Fig. 1, the door is positioned closer to the eastern wall, allowing recirculation zones to form further to the entrance and difficulting the air exchange for the NW wind case.

The most effective ventilation occurs in the autumn simulation, which demonstrates a notable reduction in average radon concentration within the LNR building. This improvement is primarily caused due to the different wind direction (S), which is directly perpendicular to the building's entrance. Despite this enhancement, radon levels in Room 1 remain elevated, as airflow through the internal door separating it from the main building remains minimal.

Analyzing the results, an important conclusion from the autumn case can be extracted. The simulated external airflow entering through the door was 0.53 m^3/s. Given the door area of 2.11 m^2 and the average introduced air velocity, an ideal flux of up to 3.71 m^3/s could be achieved. This means that only the 14 % of this expected airflow is obtained, indicating inefficient ventilation. This inefficiency arises from the lack of an additional exit point for the inside air. With only a single opening, air movement is restricted, significantly reducing ventilation efficiency. Introducing a secondary opening, such as a window or an additional door, would greatly enhance ventilation by providing a clear circulation path for air to exit. This improvement would be beneficial not only in the autumn scenario but also across all seasonal conditions, where the inclusion of a door at the northern wall of the building would dramatically improve the airflow inside the building.

The comparison of ACH values from Table 6 between Room 1 and the entire LNR building reveals consistent behavior for three of the four simulated seasons. In winter, spring, and summer, the ventilation rates inside Room 1 are comparable to those of the overall building,

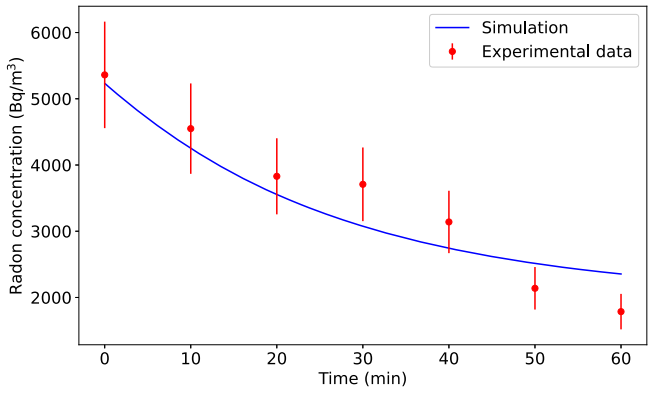

Fig. 7. Comparison between the experimental data for the forced ventilation methodology and the simulated data. Simulated data corresponds to the average radon concentration within Room 1.

with only minor differences. This indicates that under these boundary conditions, the air exchange within the building is uniformly limited, and the restricted inflow of outdoor air affects both the local (Room 1) and global (LNR) environments in a comparable manner. The situation changes in the autumn case, where the ACH for the whole building increases sharply to 1.11 h^{-1}—more than four times higher than in the other seasons—while Room 1 reaches only 0.25 h^{-1}. This pronounced disparity highlights the poor internal air communication between Room 1 and the rest of the LNR. Despite the improved external ventilation caused by the perpendicular wind direction to the entrance, the limited airflow through the interior doorway prevents the efficient renewal of air in Room 1. Consequently, the room remains largely isolated from the building's overall ventilation dynamics. This behavior underscores the importance of internal connectivity and cross-ventilation pathways: even when external conditions promote higher overall air exchange, confined subspaces with restricted openings may continue to exhibit elevated radon concentrations.

Given that radon concentrations remained elevated under the evaluated setups, particularly in Room 1, the next step involves implementing a forced ventilation system to enhance the intake of fresh air, as described in the previous section. During the measurement time interval, wind conditions were characterized by a predominant northeast (NE) component, comparable to those observed in the winter and spring cases and with similar wind speeds. In those earlier simulations, natural ventilation alone failed to significantly reduce radon levels. However, they serve as useful reference points for evaluating the effectiveness of forced ventilation, which can now serve us to validate our simulations using the corresponding experimental data.

The results of this comparison are presented in Fig. 7, which displays both the simulation outcomes and the corresponding experimental measurements. As shown, the simulated radon concentrations closely follow the trend observed in the experimental data. Minor discrepancies between the two can be attributed to factors such as limitations in the fan modeling and the use of boundary conditions that may lack sufficient accuracy. It is also worth noting that the meteorological data was obtained from a station located over 4 km away from the laboratory, which could lead to deviations in wind-related parameters. Additionally, the simulations assumed a constant average wind speed and radon exhalation rate, while in reality, meteorological conditions likely varied throughout the experiment. This variation helps explain why the data does not follow a perfect exponential trend, showing instead a slight deviation around the midpoint of the measurement period. Despite these considerations, the overall agreement between simulation and experiment supports the validity of the simulation methodology.

We can see that forced ventilation proves to be a highly effective strategy for reducing radon concentrations, particularly under conditions where wind is weak and air inlets are insufficient. In fact, it is the only scenario in which radon levels in Room 1 are reduced, whereas all other cases exhibit a continuous increase in concentration. This is also supported by the ACH value calculated for this simulation, going up to 2.21 h^{-1} for the Room 1 (more than 10 times higher than in the seasonal studies with natural ventilation) and 0.67 h^{-1} to the whole building. This higher value for Room 1 can be expected, as the clean air intake is directed into the room. The amount of wind entering the building is comparable to the seasonal cases with NE wind direction, and the greater λ_{ACH} value in comparison with the other cases is explained by the inclusion of the fan inside Room 1, which also introduces clean air inside one part of the building. After one hour, the average radon concentration stands just above 2,000 Bq/m^3, while in the natural ventilation cases, radon levels reached between 8000 and 10,000 Bq/m^3. This corresponds to four times greater values, demonstrating once again the effectiveness of forced ventilation setups under sub-optimal ventilation conditions.

3.1. Engineering applications

The methodology and findings of this study provide key insights for the design and assessment of radon mitigation systems in buildings with limited ventilation. The presented framework enables engineers to predict radon accumulation patterns and evaluate ventilation strategies before implementation.

The results presented here demonstrate that effective radon mitigation strongly depends on the existence of cross-ventilation paths. Even with favorable external airflow, a single opening significantly limits the renewal of indoor air. Introducing a secondary outlet substantially enhances air circulation by providing a clear exit pathway for the air, as demonstrated by our results. In practice, this simple modification can transform an inefficient ventilation scheme into an effective mitigation strategy, particularly in underground or semi-enclosed spaces.

The forced ventilation system proved highly effective, increasing the ACH more than tenfold compared with natural ventilation and markedly reducing radon concentrations. The close match between simulated and experimental radon data—typically within the measurement uncertainty—further supports the accuracy of the modeling approach. Although our results pertain to a specific test building, the methodology is broadly applicable to other structures with limited ventilation or elevated radon potential.

From an engineering perspective, our CFD-based methodology offers an efficient way to optimize the placement of air inlets, outlets, or fans within existing or planned structures. Its scalability allows it to be applied to more complex geometries or larger facilities without prohibitive computational costs. Beyond radon mitigation, the same framework can be extended to a wide range of indoor air quality assessments, including studies of pollutant dispersion, humidity control, and thermal comfort in enclosed spaces. By accurately reconstructing both indoor and outdoor flow domains, the method improves the definition of boundary conditions, enhancing the reliability of ventilation simulations. As such, it bridges environmental modeling and practical engineering design, offering a robust foundation for improving air quality management in low-ventilation environments.

4. Conclusions

Accumulation of radon within indoor spaces has become a recognized health problem worldwide, and various official organizations have started to impose restrictions on radon concentration levels, mainly in enclosed spaces such as houses or workplaces. To keep up with this trend, it is important to know how different mitigation methodologies affect indoor radon concentrations.

In this context, experimental measurements of radon concentrations over time were conducted in the Laboratory of National Radiation (LNR), a unique experimental facility located in a former uranium mine in Saelices el Chico (Salamanca, Spain). Radon measurements in Room

1 were used to determine a representative radon generation rate under worst-case conditions, which was subsequently applied in a series of simulations modeling natural ventilation under predominant seasonal wind conditions

Results show that natural ventilation alone is insufficient to reduce radon effectively, especially in poorly connected subspaces such as Room 1. Across winter, spring, and summer scenarios, only minor differences in average radon concentration appeared, reflecting limited air exchange due to the building internal layout. In autumn, when wind was perpendicular to the entrance, overall ventilation improved but airflow through the internal doorway to Room 1 remained minimal. Quantitative analysis of Air Changes per Hour (ACH) highlighted this disparity: the LNR building reached 1.11 h^{-1} in autumn, while Room 1 reached only 0.25 h^{-1} (a reduction of near 80 %), demonstrating the critical role of internal connectivity and cross-ventilation pathways.

In the literature, an ACH of 0.5-1 h^{-1} is often treated as a useful reference point. For instance, [38] and [31] report that maintaining 1 ACH keeps radon concentrations within acceptable limits, while lower rates cause sharp increases. In our study, forced ventilation in Room 1 achieved 2.21 h^{-1}, comfortably above this benchmark. Natural ventilation cases yielded only 0.13–0.25 h^{-1}, confirming that single-opening configurations are inadequate in this suboptimal setup. Thus, we can conclude that effective mitigation in confined subspaces requires at least 1–2 h^{-1} of ventilation.

Despite these promising results, some limitations must be noted. The radon generation rate $G(t)$ was treated as a constant, fitted linearly while neglecting the baseline component. With measurements obtained from an initially radon-free room, it would be possible to better distinguish between the baseline and the meteorologically driven components of radon generation. Moreover, the analysis was carried out under worst-case conditions, which in practice may only persist for a couple hours. Also, in most real situations the generation rate is likely much lower or even negative depending on the variations of external conditions. No experimental data were available for the natural ventilation scenarios, limiting the validation of the simulations. Additionally, the fan performance curve used in the mechanical ventilation modeling had to be approximated from a similar device, introducing some uncertainty in the estimation of volumetric airflow. Finally, although the methodology of environmental reconstruction was validated under forced ventilation, its performance in more complex geometries or highly turbulent environments remains to be fully verified, even though it was already tested successfully in [33].

From a computational perspective, the CFD framework was very efficient. Steady-state outdoor simulations were run in less than one hour on a standard workstation, showing feasibility for realistic case studies. Extending to larger and more complex regions would increase the overall computational cost, but it could be managed by focusing on critical high-radon areas while simplifying peripheral zones. This scalability supports broader applicability for radon risk assessment, air quality studies, and mitigation design, as stated in the previous section.

Future work will focus on addressing these limitations by improving experimental measurements to validate the proposed methodology in more complex environments—such as multi-room buildings with internal walls or irregular layouts—and by refining the estimation of $G(t)$ to separate baseline emission from the meteorological contribution. Moreover, extending the dataset to include transient measurements of radon decay under natural ventilation would allow for more comprehensive validation of the modeling framework. These advances will strengthen the predictive capability of the CFD methodology and support the design of robust, energy-efficient mitigation strategies for buildings affected by radon accumulation.

CRediT authorship contribution statement

Marcos Suárez-Vázquez: Writing – original draft, Visualization, Software, Methodology, Investigation, Formal analysis, Data curation, Conceptualization; **Vanesa Somoza:** Software, Methodology; **Sylvana Varela Ballesta:** Writing – review & editing, Supervision, Resources, Investigation, Formal analysis, Data curation, Conceptualization; **Alberto Otero-Cacho:** Writing – review & editing, Validation, Supervision, Resources, Methodology, Funding acquisition, Conceptualization; **Alberto P. Muñuzuri:** Writing – review & editing, Validation, Supervision, Resources, Methodology, Funding acquisition, Conceptualization; **Daniel Rábago:** Writing – review & editing, Supervision, Resources, Data curation; **Santiago Celaya:** Writing – review & editing, Supervision, Resources, Data curation; **Jorge Mira:** Writing – review & editing, Validation, Supervision, Resources, Project administration, Methodology, Funding acquisition, Conceptualization.

Data availability

Data will be made available on request.

Declaration of competing interest

The authors declare that they have no known competing financial interests or personal relationships that could have appeared to influence the work reported in this document.

Acknowledgments

M. Suárez-Vázquez thanks the support of the Doutoramento Industrial program from GAIN-Xunta de Galicia (IN606D).

Supplementary material

Supplementary material associated with this article can be found in the online version at 10.1016/j.rineng.2025.108483

References

[1] L.J.R. Nunes, A. Curado, S.I. Lopes, The relationship between radon and geology: sources, transport and indoor accumulation, Appl. Sci. 13 (13) (2023) 7460. https://doi.org/10.3390/app13137460
[2] W.C. Burnett, Radon Tracing of Submarine Groundwater Discharge in Coastal Environments. Land and Marine Hydrogeology, 2003. https://doi.org/10.1016/b978-044451479-0/50015-7
[3] L.D. Cecil, J.R. Green, Radon-222, in: Environmental Tracers in Subsurface Hydrology, Springer, 2000, pp. 175–194. https://doi.org/10.1007/978-1-4615-4557-6_6
[4] S. Tokonami, Characteristics of thoron (220rn) and its progeny in the indoor environment, Int. J. Environ. Res. Public Health 17 (23) (2020) 8769. https://doi.org/10.3390/ijerph17238769
[5] M. Riudavets, M.G.D. Herreros, B. Besse, L. Mezquita, Radon and lung cancer: current trends and future perspectives, Cancers 14 (13) (2022) 3142. https://doi.org/10.3390/cancers14133142
[6] WHO handbook on indoor radon: a public health perspective, World Health Organization, 2009.
[7] S. Darby, D. Hill, A. Auvinen, J.M. Barros-Dios, H. Baysson, F. Bochicchio, H. Deo, R. Falk, et al., Radon in homes and risk of lung cancer: collaborative analysis of individual data from 13 european case-control studies, BMJ 330 (7485) (2005) 223. https://doi.org/10.1136/bmj.38308.477650.63
[8] C.J.L. Murray, A.Y. Aravkin, P. Zheng, C. Abbafati, K.M. Abbas, M. Abbasi-Kangevari, F. Abd-Allah, et al., Global burden of 87 risk factors in 204 countries and territories, 1990–2019: a systematic analysis for the global burden of disease study, Lancet 396 (2019) 1223–1249. https://doi.org/10.1016/S0140-6736(20)30752-2
[9] M. Ćujić, L.J. Mandić, J. Petrović, R. Dragović, M. Đorđević, M. Đokić, S. Dragović, Radon-222: environmental behavior and impact to (human and non-human) biota, Int. J. Biometeorol. 65 (2021) 69–83. https://doi.org/10.1007/s00484-020-01860-w
[10] Which establishes the technical-sanitary criteria for the quality of water for human consumption, its control and supply, 8, 2023. Royal Decree 3/2023, https://www.boe.es/eli/es/rd/2023/01/10/3.
[11] M. Janik, Y. Omori, H. Yonehara, Influence of humidity on radon and thoron exhalation rates from building materials, Appl. Radiat. Isot. 95 (2015) 102–107. https://doi.org/10.1016/j.apradiso.2014.10.007
[12] M. Kumar, N. Sharma, A. Sarin, Prediction of indoor radon/thoron concentration in a model room from exhalation rates of building materials for different ventilation rates, Acta Geophys. 66 (5) (2018) 1249–1255. https://doi.org/10.1007/s11600-018-0159-5
[13] United nations scientific committee on the effects of atomic radiation (UNSCEAR), Un Sci. Committee Rep. i (2000). Sources of Ionizing Radiation.

[14] Euratom of 5 December 2013 Laying Down Basic Safety Standards for Protection Against the Dangers Arising from Exposure to Ionising Radiation, European Union. Council Directive, 2013. https://eur-lex.europa.eu/legal-content/EN/TXT/?uri=CELEX.
[15] Radon - a barely perceived risk, German Federal Office for Radiation Protection (BfS), 2024. https://www.bfs.de/SharedDocs/Downloads/BfS/EN/brochures/stko-radon-en.pdf?blob=publicationFile&v=9.
[16] Radon Action Level and Target Level, UK Health Security Agency, 2025. https://www.ukradon.org/information/level.
[17] G.O. Spain, Royal Decree 1029/2022 of 20 December, approving the Regulation on Health Protection Against Risks Arising from Exposure to Ionizing Radiation, 2022. https://www.boe.es/buscar/act.php?id=BOE-A-2022-21682.
[18] Mapa del potencial de radón en España, Consejo de Seguridad Nuclear, 2017. https://www.csn.es.
[19] WHO Guidelines for Indoor Air Quality: Selected Pollutants. World Health Organization, World Health Organization, 2010. https://www.who.int/publications/i/item/9789241547628.
[20] D.B. Henschel, Analysis of radon mitigation techniques used in existing US houses, Radiat. Prot. Dosimetry 56 (1–4) (1994) 21–27. https://doi.org/10.1093/oxfordjournals.rpd.a082416
[21] A. Cavallo, K. Gadsby, T.A. Reddy, Comparison of natural and forced ventilation for radon mitigation in houses, Environ. Int. 22 (1996) 1073–1078. https://doi.org/10.1016/s0160-4120(96)00221-8
[22] C.E. Andersen, N.C.B. e, B. Majborn, K. Ulbak, Radon and natural ventilation in newer danish single-Family houses, Indoor Air 7 (4) (1997) 278–286. https://doi.org/10.1111/j.1600-0668.1997.00007.x
[23] K. Akbari, J. Mahmoudi, M. Ghanbari, Simulation of ventilation effects on indoor radon, Manage. Environ. Qual.: Int. J. 24 (3) (2013) 394–407. https://doi.org/10.1108/14777831311322686
[24] K.A. Landman, Diffusion of radon through cracks in a concrete slab, Health Phys. 43 (1) (1982) 65–71. https://doi.org/10.1097/00004032-198207000-00006
[25] M. Fuente, D. Rábago, J. Goggins, I. Fuente, C. Sainz, M. Foley, Radon mitigation by soil depressurisation case study: radon concentration and pressure field extension monitoring in a pilot house in spain, Sci. Total Environ. 695 (2019) 133746. https://doi.org/10.1016/j.scitotenv.2019.133746
[26] J. Gaskin, L.G. Zhou, Y.E. Li, P. Tardif, Ventilation approaches and radon control in canadian houses, Front. Public Health 13 (2025) 1569494. https://doi.org/10.3389/fpubh.2025.1569494
[27] R. Parkash, N. Chauhan, R.P. Chauhan, Application of CFD modeling for indoor radon and thoron dispersion study: a review, J. Environ. Radioact. 272 (2024) 107368. https://doi.org/10.1016/j.jenvrad.2023.107368
[28] P.M. Dieguez-Elizondo, T. Gil-Lopez, P.G. O'donohoe, J. Castejon-Navas, M.A. Galvez-Huerta, An analysis of the radioactive contamination due to radon in a granite processing plant and its decontamination by ventilation, J. Environ. Radioact. 167 (2017) 26–35. https://doi.org/10.1016/j.jenvrad.2016.11.016
[29] R. Rabi, L. Oufni, Study of radon dispersion in typical dwelling using CFD modeling combined with passive-active measurements, Radiat. Phys. Chem. 139 (2017) 40–48. https://doi.org/10.1016/j.radphyschem.2017.04.012
[30] N. Chauhan, R.P. Chauhan, M. Joshi, T.K. Agarwal, P. Aggarwal, B.K. Sahoo, Stoor radon distribution using measurements and CFD modeling, J. Environ. Radioact. 136 (2014) 105–111. https://doi.org/10.1016/j.jenvrad.2014.05.020
[31] J.E. Lee, H.C. Park, H.S. Choi, S.Y. Cho, T.Y. Jeong, S.C. Roh, A numerical study on the performance evaluation of ventilation systems for indoor radon reduction, Korean J. Chem. Eng. 33 (3) (2016) 782–794. https://doi.org/10.1007/s11814-015-0214-8
[32] R. Rabi, L. Oufni, E. Youssoufi, K. Cheikh, H. Badry, Y. Errami, CFD Simulation and experimental measurements of radon distribution in a traditional hammam, Int. J. Heat Technol. 39 (2021) 963–968. https://doi.org/10.18280/ijht.390333
[33] M. Suárez-Vázquez, S.V. Ballesta, A. Otero-Cacho, A.P.M. nuzuri, J. Mira, A fast and automated approach for urban cfd simulations: validation with meteorological predictions and its application to drone flights, 64, Urban Climate, 2025 https://doi.org/10.1016/j.uclim.2025.102664
[34] Simcenter STAR-CCM User Guide, 2410.0001 (19.06.009, Siemens Digital Industries Software, 2024
[35] J.H. Ferziger, M. Perić, Computational Methods for Fluid Dynamics, Springer, Berlin Heidelberg, 2019. https://doi.org/10.1007/978-3-642-56026-2
[36] C. Teodosiu, V. Ilie, R. Teodosiu, Appropriate CFD turbulence model for improving indoor air quality of ventilated spaces, Math. Model. Civil Eng. 10 (4) (2014). https://doi.org/10.2478/mmce-2014-0020
[37] D. Altendorf, H. Wienkenjohann, F. Berger, J. Dehnert, H. Grünewald, D. Naumov, R. Trabitzsch, H. Weiß, Successful reduction of indoor radon activity concentration via cross-ventilation: experimental data and CFD simulations, Isotopes Environ. Health Stud. 60 (1) (2024) 74–89. https://doi.org/10.1080/10256016.2023.2282686
[38] M. Adelikhah, M. Imani, T. Kovács, Measurements and computational fluid dynamics investigation of the indoor radon distribution in a typical naturally ventilated room, Sci. Rep. 13 (1) (2023) 2064. https://doi.org/10.1038/s41598-022-23642-7
[39] W. Rodi, Experience with two-layer models combining the k-epsilon model with a one-equation model near the wall, in: 29th Aerospace Sciences Meeting, 1991, p. 216. https://doi.org/10.2514/6.1991-216
[40] J.L. Peter, G.M. William, NIST Chemistry WebBook, NIST Standard Reference Database Number 69, Technical Report, National Institute of Standards and Technology, 2024. https://webbook.nist.gov/chemistry/.
[41] S. Sarkar, B. Lakshmanan, Application of a reynolds stress turbulence model to the compressible shear layer, AIAA J. 29 (5) (1991) 743–749. https://doi.org/10.2514/6.1990-1465
[42] M. Fuente, D. Rabago, S. Herrera, L. Quindos, I. Fuente, M. Foley, C. Sainz, Performance of radon monitors in a purpose-built radon chamber, J. Radiol. Prot. 38 (3) (2018) 1111. https://doi.org/10.1088/1361-6498/aad969
[43] T.R. Beck, A. Antohe, F. Cardellini, A. Cucoş, E. Fialova, C. Grossi, K. Hening, J. Jensen, D. Kastratović, M. Krivošík, et al., The metrological traceability, performance and precision of european radon calibration facilities, Int. J. Environ. Res. Public Health 18 (22) (2021) 12150. https://doi.org/10.3390/ijerph182212150
[44] A. Röttger, S. Röttger, D.R. Gómez, L.Q. Poncela, K. Woloszczuk, M. Norenberg, I. Radulescu, A. Luca, et al., Metrology infrastructure for radon metrology at the environmental level. IMEKO, 2023 https://doi.org/10.21014/actaimeko.v12i2.1440
[45] International Organization for Standardization. ISO/IEC 17025:2017 - General Requirements for the Competence of Testing and Calibration Laboratories, Technical Report, ISO, Geneva, Switzerland, 2017.
[46] D. Rábago, E. Fernández, S. Celaya, I. Fuente, A. Fernández, J. Quindós, R. Rodriguez, L. Quindós, C. Sainz, Investigation of the performance of various low-Cost radon monitors under variable environmental conditions, Sensors 24 (6) (2024) 1836. https://doi.org/10.3390/s24061836
[47] F. Cardellini, P.D. Felice, M. Pagliari, Determination of blank indication of active radon monitors, Appl. Radiat. Isot. 81 (2013) 242–247. https://doi.org/10.1016/j.apradiso.2013.03.093
[48] G. Butterweck-Dempewolf, C. Schuler, An extended radon chamber model, Environ. Int. 22 (1996) 891–898.
[49] D. Xie, M. Liao, K.J. Kearfott, Influence of environmental factors on indoor radon concentration levels in the basement and ground floor of a building-A case study, Radiat. Meas. 82 (2015) 52–58. https://doi.org/10.1016/j.radmeas.2015.08.008
[50] P. Huang, W. Lv, R. Huang, Y. Feng, Q. Luo, C. Yin, Y. Yang, Impact of environmental factors on atmospheric radon variations at china jinping underground laboratory, Sci. Rep. 14 (1) (2024) 31402. https://doi.org/10.1038/s41598-024-82936-0
[51] K. Singh, M. Singh, S. Singh, H.S. Sahota, Z. Papp, Variation of radon (rn) progeny concentrations in outdoor air as a function of time, temperature and relative humidity, Radiat. Meas. 39 (2) (2005) 213–217. https://doi.org/10.1016/j.radmeas.2004.06.015
[52] P. Zippenfenig, Open-meteo.com weather api, 2023. CC-BY-4.0 license, https://open-meteo.com/. https://doi.org/10.5281/zenodo.7970649
[53] B. Blocken, Computational fluid dynamics for urban physics: importance, scales, possibilities, limitations and ten tips and tricks towards accurate and reliable simulations, Build. Environ. 91 (2015) 219–245. https://doi.org/10.1016/j.buildenv.2015.02.015
[54] A. Parente, C. Gorlé, J.V. Beeck, C. Benocci, Improved k-epsilon model and wall function formulation for the RANS simulation of ABL flows, J. Wind Eng. Ind. Aerodyn. 99 (4) (2011) 267–278. https://doi.org/10.1016/j.jweia.2010.12.017
[55] E.L. Andreas, K.J. Claffey, R.E. Jordan, C.W. Fairall, P.S. Guest, P.O.G. Persson, A.A. Grachev, Evaluations of the von kármán constant in the atmospheric surface layer, J. Fluid Mech. 559 (2006) 117–149. https://doi.org/10.1017/s0022112006000164
[56] J. Wieringa, Updating the davenport roughness classification, J. Wind Eng. Ind. Aerodyn. 41 (1–3) (1992) 357–368. https://doi.org/10.1016/0167-6105(92)90434-c